Pattern dynamics in rotating convection at finite Prandtl number

Y. Ponty, T. Passot, and P. L. Sulem

CNRS UMR 6529, Observatoire de la Côte d'Azur, Boîte Postale 4229, 06304 Nice cedex 4, France

(Received 24 March 1997)

A Swift-Hohenberg-type model is derived for rotating convection in a Boussinesq fluid at a moderate Prandtl number, for both free-slip and rigid top and bottom boundary conditions. In the former case, a phase dynamics analysis is used to relate the skewed-varicose instability, which can occur in the absence of rotation, and the small-angle instability which develops for arbitrary rotation rate and leads to a continuous rotation of the rolls. Numerical simulations show the ordering effect of a moderate rotation which counterbalances the destructuring effect of the mean flow. In the free-slip case, this effect induces the formation of coherent targets, associated with large vortices of the same sign as the external rotation. In the no-slip case, this leads to a maximum correlation of the patterns for a rotation rate of the order of the critical value for the onset of the Küppers-Lortz instability. [S1063-651X(97)12509-0]

PACS number(s): 47.27.Te, 47.20.Lz, 47.52.+j, 47.54.+r

I. INTRODUCTION

In addition to its relevance in the context of astrophysical and geophysical fluid dynamics, rotating convection provides a prototype to study the transition to spatiotemporal chaos [1]. The reason is that, close to onset, a chaotic dynamics can result from the destabilization of the basic patterns through the Küppers-Lortz (KL) instability [2–5]. It turns out that, at a finite Prandtl number, special dynamical features can appear. With free-slip boundaries, due to the presence of an intense mean flow, straight parallel rolls have been shown to be linearly unstable relative to a small-angle instability for any value of the rotation rate [6]. With rigid boundaries, experiments in cylindrical boxes have also revealed that the KL instability can arise below the critical rotation, a phenomenon attributed to the influence of sidewall defects [7,8]. A recent thorough experimental study of convective patterns with moderate rotation [9] demonstrated the richness of the system, and pointed out a number of still unresolved questions that deserve theoretical and numerical investigation.

Several models in the spirit of the Swift-Hohenberg equation have been built in the limit of the infinite Prandtl number [10–12]. In this regime, the main observation is that when the Taylor number Ta exceeds the critical value for the Küppers-Lortz instability, the destabilization of straight parallel rolls (which arises as soon as the Rayleigh number R exceeds the convection threshold R_c), leads to the formation of patches of straight rolls penetrating each other in a chaotic way: rolls disappear and are replaced by other rolls tilted by an angle close to 60°.

The aim of the present paper is to address the problem of rotating convection at a moderate Prandtl number, taken larger than the critical value (0.677 in the case of free-slip boundary conditions), above which overstability is not possible and the convective instability leads (near onset) to the formation of steady straight parallel rolls [13]. In Sec. II, a model is derived in the context of both rigid and free-slip top and bottom boundary conditions, whose strong influence on the mean flow significantly affects the dynamics. In horizontal directions, the flow is assumed to be periodic. It improves

a model given in Ref. [14] in the case of rigid boundaries, by the inclusion of additional couplings, and by a better prescription of the coefficients, resulting in more accurate values for the KL instability threshold.

The phase dynamics is analyzed in Sec. III where, in the case of free-slip boundaries, particular attention is paid to the relation between the small-angle instability and the skewed varicose instability which can arise in the absence of rotation [15,16]. In the fully nonlinear regime, a main conclusion concerns the relaminarization which takes place for rotation rates comparable to the critical rotation for the onset of the Küppers-Lortz instability. In the case of free-slip boundaries (Sec. IV), this effect leads to the formation of coherent targets and vortices. With rigid boundaries (Sec. V), dislocations can totally annihilate each other, and lead to the stabilization of straight parallel rolls. Section VI briefly summarizes the main results.

II. A MODEL FOR ROTATING CONVECTION

A. An asymptotic model near threshold for free-slip boundaries

The Boussinesq equations in a horizontal fluid layer heated from below and rotating around a vertical axis $\hat{\mathbf{z}}$ are written in the nondimensional form

$$\Delta \mathbf{V} + \hat{\mathbf{z}}\theta - \nabla\Gamma - \tau\hat{\mathbf{z}}\times\mathbf{V} = P^{-1}(\mathbf{V}\cdot\nabla\mathbf{V} + \partial_t\mathbf{V}), \quad (2.1)$$

$$\nabla\cdot\mathbf{V} = 0, \quad (2.2)$$

$$\Delta\theta + R\hat{\mathbf{z}}\cdot\mathbf{V} = \mathbf{V}\cdot\nabla\theta + \partial_t\theta, \quad (2.3)$$

where the vertical diffusion time is taken as time unit. The other parameters are the Rayleigh number R and the square root τ of the Taylor number (twice the Rossby number) which, to be specific, is taken to be positive.

It is convenient to rewrite the velocity field $\mathbf{V}=(\mathbf{u},w)$ in terms of a potential ϕ and a stream function ψ, in the form

$$\mathbf{u}=(u,v)=(\nabla_h\phi-\mathbf{e}_z\times\nabla_h\psi),\qquad(2.4)$$

$$\Delta_h\phi=-\partial_z w,\qquad(2.5)$$

where the subscript h refers to the horizontal directions. Applying successively the operators curl and curl^2 on Eq. (2.1), and projecting the resulting equations on the vertical axis, we obtain

$$(\partial_t-P\Delta)\Delta_h\psi=-\tau P\partial_z w+\partial_x(\mathbf{V}\cdot\nabla v)-\partial_y(\mathbf{V}\cdot\nabla u),$$
$$(2.6)$$

$$P^{-1}(\partial_t\Delta w+\mathcal{Q}_1)=\Delta^2 w+\Delta_h\theta+\tau\partial_z\Delta_h\psi,\qquad(2.7)$$

with

$$\mathcal{Q}_1=\Delta_h(\mathbf{V}\cdot\nabla w)-\partial_z[\partial_x(\mathbf{V}\cdot\nabla u)+\partial_y(\mathbf{V}\cdot\nabla v)].\quad(2.8)$$

Applying the operators $(\partial_t-\Delta)$ to Eq. (2.7), Δ_h to Eq. (2.3), and $-\tau P^{-1}\partial_z$ to Eq. (2.6), and summing the resulting equations, we obtain

$$-P^{-1}\partial_{tt}^2\Delta w+(1+P^{-1})\partial_t\Delta^2 w+\mathcal{Q}_2$$
$$=\Delta^3 w-R\Delta_h w+\tau^2\partial_{zz}w-\tau(1-P^{-1})\partial_z\partial_t\Delta_h\psi,\qquad(2.9)$$

where

$$\mathcal{Q}_2=P^{-1}(\Delta-\partial_t)\mathcal{Q}_1-\Delta_h(\mathbf{V}\cdot\nabla\theta)+\tau P^{-1}\partial_z[\partial_x(\mathbf{V}\cdot\nabla v)$$
$$-\partial_y(\mathbf{V}\cdot\nabla u)].\qquad(2.10)$$

As already mentioned, we assume that the Prandtl number exceeds the minimum value $P^*\approx0.677$ for which, in the case of free-slip boundary conditions, the convective instability first sets in as stationary convection, and define the stress parameter $\epsilon=(R-R_c)/R_c$ where R_c is the critical Rayleigh number. Denoting the critical wave number by q_c, we have [13]

$$R_c=[\tau^2\pi^2+(\pi^2+q_c^2)^3]/q_c^2,\qquad(2.11)$$

with q_c given by

$$2q_c^6+3\pi^2q_c^4=\pi^6+\pi^2\tau^2.\qquad(2.12)$$

Near threshold, we perform the Galerkin expansion

$$w=w_1\sin\pi z+w_2\sin2\pi z+\cdots,\qquad(2.13)$$

$$\phi=\phi_1\cos\pi z+\phi_2\cos2\pi z+\cdots,\qquad(2.14)$$

$$\psi=\psi_0+\psi_1\cos\pi z+\psi_2\cos2\pi z+\cdots,\qquad(2.15)$$

$$\theta=\theta_1\sin\pi z+\theta_2\sin2\pi z+\cdots,\qquad(2.16)$$

where w_1, ϕ_1, ψ_0, ψ_1, and θ_1 are of order $\epsilon^{1/2}$, while w_2, ϕ_2, ψ_2, and θ_2 are of order ϵ. Furthermore, time derivatives are assumed to be of order ϵ. The horizontal structure is left unspecified, in order to preserve isotropy. We nevertheless assume that the pattern can locally be viewed as a superposition of slowly modulated rolls with critical wave number

q_c. When acting on a field locally periodic in the horizontal variables, the Laplacian operator Δ_h thus reduces, to leading order, to the multiplication by $-q_c^2$. The horizontal gradient ∇_h is of order one in the direction across the roll and of order $\epsilon^{1/4}$ in the direction along the roll. Since the direction of the structure is not specified, ∇_h must in general be considered of order unity. However, when acting on slowly varying quantities, ∇_h will be of order $\epsilon^{1/4}$ and Δ_h of order $\epsilon^{1/2}$, as used in Ref. [17]. We thus write $\Delta_h w_1=(-q_c^2+\mathcal{L})w_1$ with $\mathcal{L}=O(\epsilon^{1/2})$. In this approach which combines an ϵ and a Galerkin expansion in the vertical direction, it turns out that subdominant terms are possibly retained at each order of approximation.

At order $\epsilon^{1/2}$, the linear analysis is recovered. Defining $q_p^2=q_c^2+\pi^2$, we have

$$-q_p^6 w_1+R_c q_c^2 w_1-\tau^2\pi^2 w_1=0,\qquad(2.17)$$

$$q_p^2 q_c^2\psi_1=\tau\pi w_1,\qquad(2.18)$$

$$q_p^2\theta_1=R_c w_1,\qquad(2.19)$$

$$q_c^2\phi_1=\pi w_1.\qquad(2.20)$$

At order ϵ, when projecting on the first Galerkin mode, we have

$$3q_p^4\mathcal{L}w_1-R_c\mathcal{L}w_1=0.\qquad(2.21)$$

At order $\epsilon^{3/2}$, using Eq. (2.18), from Eq. (2.7) we obtain

$$3q_p^2 q_c^2\left[1+\frac{1}{P}\left(1-\frac{2\tau^2\pi^2}{R_c q_c^2}\right)\right]\partial_t w_1=(\epsilon q_c^2 R_c-3q_p^2\mathcal{L}^2)w_1-\mathcal{Q}.$$
$$(2.22)$$

The nonlinear term $\mathcal{Q}$ stands for the $\epsilon^{3/2}$ contribution arising from the quantity $\mathcal{Q}_2$ defined in Eq. (2.10), when projected on $\sin\pi z$. After straightforward algebra, we obtain

$$\mathcal{Q}=P^{-1}(\Delta_h-\pi^2)\Delta_h\left[(\mathbf{u_0}\cdot\nabla_h w_1)+\frac{1}{2}(\mathbf{u_1}\cdot\nabla_h w_2-\mathbf{u_2}\cdot\nabla_h w_1)\right.$$

$$-\frac{\pi}{2}(w_1 w_2)\right]+\pi P^{-1}[(\Delta_h-\pi^2)\nabla_h\cdot-\tau\mathbf{e_z}\cdot\nabla_h]$$

$$\times\left[(\mathbf{u_1}\cdot\nabla_h\mathbf{u_0}+\mathbf{u_0}\cdot\nabla_h\mathbf{u_1})+\frac{1}{2}(\mathbf{u_1}\cdot\nabla_h\mathbf{u_2}+\mathbf{u_2}\cdot\nabla_h\mathbf{u_1})\right.$$

$$\left.-\frac{\pi}{2}(w_2\mathbf{u_1}+2w_1\mathbf{u_2})\right]-\Delta_h\left[3q_p^2\mathbf{u_0}\cdot\nabla_h w_1+\frac{1}{2}(\mathbf{u_1}\cdot\nabla_h\theta_2\right.$$

$$\left.-3q_p^2\mathbf{u_2}\cdot\nabla_h w_1)-\left(\pi w_1\theta_2+\frac{3\pi}{2}q_p^2 w_1 w_2\right)\right]\qquad(2.23)$$

where, writing $\beta=\tau/q_p^2$, we defined

$$\mathbf{u_0}=\begin{pmatrix}\partial_y\psi_0\\-\partial_x\psi_0\end{pmatrix},\qquad(2.24)$$

$$\mathbf{u_1}=\frac{\pi}{q_c^2}\begin{pmatrix}\partial_x w_1+\beta\partial_y w_1\\\partial_y w_1-\beta\partial_x w_1\end{pmatrix},\qquad(2.25)$$

$$\mathbf{u_2} = \begin{pmatrix} \partial_x \phi_2 + \partial_y \psi_2 \\ \partial_y \phi_2 - \partial_x \psi_2 \end{pmatrix}, \qquad (2.26)$$

and neglected terms involving derivatives of the slowly varying field $\mathbf{u_0}$.

Similarly, the contribution of order ϵ to the projection of Eq. (2.7) on $\sin 2\pi z$ reads

$$(\Delta_h - 4\pi^2)^2 w_2 + \Delta_h \theta_2 - 2\pi\tau\Delta_h\psi_2$$
$$= \frac{q_p^2 \pi}{2Pq_c^4}\Delta_h\mathcal{M} + \frac{\pi^3}{Pq_c^4}\beta\mathcal{N} - \frac{2\pi^3}{Pq_c^4}\beta^2\mathcal{H}, \qquad (2.27)$$

where

$$\mathcal{M} = (\nabla_h w_1)^2 + q_c^2 w_1^2, \qquad (2.28)$$

$$\mathcal{N} = [\nabla_h(\Delta_h w_1) \times \nabla_h w_1] \cdot \mathbf{e}_z, \qquad (2.29)$$

$$\mathcal{H} = \partial_{xx} w_1 \partial_{yy} w_1 - (\partial_{xy} w_1)^2. \qquad (2.30)$$

From Eqs. (2.3) and (2.6), we have, at this order,

$$(\Delta_h - 4\pi^2)\theta_2 + R_c w_2 = \frac{3\pi}{2}\frac{q_p^2}{q_c^2}\mathcal{M}, \qquad (2.31)$$

$$(\Delta_h - 4\pi^2)\Delta_h\psi_2 - 2\pi\tau w_2 = \frac{\beta\pi^2}{2Pq_c^4}\Delta_h\mathcal{M} - \frac{\pi^2}{2Pq_c^4}(1-\beta^2)\mathcal{N}$$
$$- \frac{2\beta\pi^2}{Pq_c^4}\mathcal{H}. \qquad (2.32)$$

Finally, the equation for the mean flow is also derived from Eq. (2.6) in the form

$$(\partial_t - P\Delta_h)\Delta_h\psi_0 = \frac{\pi^2}{2q_c^4}(1-\beta^2)\mathcal{N} - \frac{\beta\pi^2}{q_c^4}[(\Delta_h w_1)^2$$
$$+ \nabla_h w_1 \cdot \nabla_h \Delta_h w_1]. \qquad (2.33)$$

Note that the term involving the time derivative is smaller by a factor $\epsilon^{1/2}$ than the other terms. It must nevertheless be kept when dealing with the large-scale, long-time dynamics. This term is particularly necessary for a uniform description of the instability growth rate of straight parallel rolls perturbed by other rolls turned by an arbitrary angle [6]. We finally obtain the set of equations

$$\tau_0\partial_t w_1 = [\epsilon - \xi_0(\Delta_h + q_c^2)^2]w_1 - g\mathcal{Q}, \qquad (2.34)$$

$$(\partial_t - P\Delta_h)\Delta_h\psi_0 = \frac{\pi^2}{2q_c^4}(1-\beta^2)\mathcal{N} - \frac{\tau\pi^2}{q_p^2 q_c^4}[(\Delta_h w_1)^2$$
$$+ \nabla_h w_1 \cdot \nabla_h \Delta_h w_1], \qquad (2.35)$$

$$\Delta_h\phi_2 = -2\pi w_2, \qquad (2.36)$$

$$\mathcal{D}\begin{pmatrix} w_2 \\ \psi_2 \\ \theta_2 \end{pmatrix} = \mathcal{F}\begin{pmatrix} \mathcal{M} \\ \mathcal{N} \\ \mathcal{H} \end{pmatrix}, \qquad (2.37)$$

with $\mathcal{Q}$ given by Eqs. (2.23)–(2.26) and $\mathcal{M}$, $\mathcal{N}$, and $\mathcal{H}$ by Eqs. (2.28)–(2.30). Furthermore,

$$\mathcal{D} = \begin{pmatrix} (\Delta_h - 4\pi^2)^2 & -2\pi\tau\Delta_h & \Delta_h \\ 2\pi\tau & -(\Delta_h - 4\pi^2)\Delta_h & 0 \\ R_c & 0 & (\Delta_h - 4\pi^2) \end{pmatrix}, \qquad (2.38)$$

$$\mathcal{F} = \begin{pmatrix} \dfrac{\pi q_p^2 \Delta_h}{2Pq_c^4} & \dfrac{\beta\pi^3}{Pq_c^4} & \dfrac{2\beta^2\pi^3}{Pq_c^4} \\[2mm] -\dfrac{\beta\pi^2\Delta_h}{2Pq_c^4} & \dfrac{(1-\beta^2)\pi^2}{2Pq_c^4} & \dfrac{2\beta\pi^2}{Pq_c^4} \\[2mm] \dfrac{3\pi}{2}\dfrac{q_p^2}{q_c^2} & 0 & 0 \end{pmatrix}, \qquad (2.39)$$

and we define the parameters

$$g = \frac{1}{q_c^2 R_c}, \quad \xi_0 = \frac{1}{q_c^2 q_p^2}, \quad \tau_0 = \frac{1}{q_p^2}\left[1 + \frac{1}{P}\left(1 - \frac{2\tau^2\pi^2}{R_c q_c^2}\right)\right]. \qquad (2.40)$$

B. Linear stability analysis

In order to validate the model derived in Sec. II A, it is of interest to compare its predictions relatively to the Küppers-Lortz instability, with the results derived from the primitive Boussinesq equations [6].

In the context of Eqs. (2.34)–(2.35), straight parallel rolls with critical wave number $|\vec{k}_1| = q_c$ are given to leading order by $w_1 = ae^{i\vec{k}_1 \cdot \vec{x}} + $c.c. and $\psi_0 = (\tau\pi^2/8q_p^2 P)a^2 e^{2i\vec{k}_1 \cdot \vec{x}} + $c.c., with an amplitude $a = \epsilon^{1/2}(1/2q_p^2[1 - (\tau^2\pi^2/q_c^4 R_c P^2)])^{-1/2}$. We consider an infinitesimal perturbation of this steady solution given to leading order by

$$\widetilde{w} = b(t)e^{i\vec{k}_2 \cdot \vec{x}} + \text{c.c.}, \qquad (2.41)$$

$$\widetilde{\psi} = h_1(t)e^{i(\vec{k}_1 - \vec{k}_2)\cdot\vec{x}} + h_2(t)e^{i(\vec{k}_1 + \vec{k}_2)\cdot\vec{x}} + \text{c.c.}, \qquad (2.42)$$

where the wave vector $\vec{k}_2$ has the same modulus as $\vec{k}_1$ and makes an angle θ with the latter. Introducing the variables $z_1 = ah_1^*$ and $z_2 = a^*h_2$, and neglecting higher-order harmonics, we obtain the linear system

$$\partial_t\begin{bmatrix} b \\ z_1 \\ z_2 \end{bmatrix} = \begin{bmatrix} \epsilon\widetilde{G}(\theta) & v_1(\theta) & v_2(\theta) \\ \epsilon p & -4q_c^2 P\sin^2\dfrac{\theta}{2} & 0 \\ \epsilon p & 0 & -4q_c^2 P\cos^2\dfrac{\theta}{2} \end{bmatrix}\begin{bmatrix} b \\ z_1 \\ z_2 \end{bmatrix} \qquad (2.43)$$
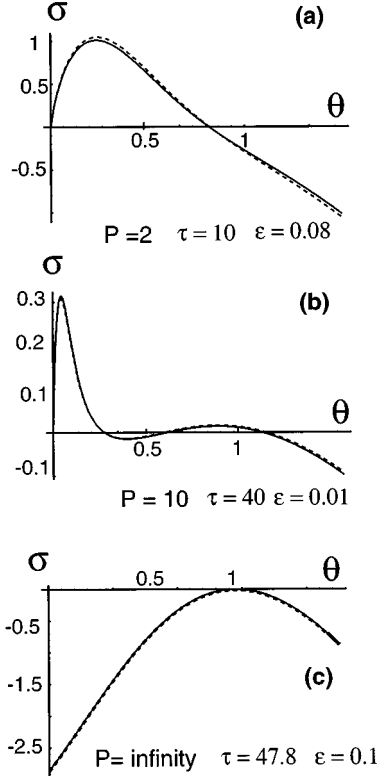
FIG. 1. Growth rate of the small-angle and Küppers-Lortz instabilities obtained from the complete model (2.34)–(2.40) (dashed line) and from the primitive Boussinesq equations (solid line), for different values of the Prandtl number P, of the Taylor number $Ta = \tau^2$ and of the stress parameter ϵ, in the case of free-slip boundary conditions.

where $p = (\tau \pi^2 / q_p^2 q_c^2)|a|^2$. The precise form of the functions $\widetilde{G}$, v_1, and v_2 was computed using MATHEMATICA software for symbolic calculations.

In the limit of infinite Prandtl number, the Küppers-Lortz instability is accurately recovered: when the rotation rate τ exceeds the critical value 47.8, two-dimensional rolls become unstable for perturbations, making an angle $\theta_c \approx 58.11°$ with the basic rolls. More generally, at a finite Prandtl number, the growth rate σ obeys

$$
- \sigma^3 + [\epsilon \widetilde{G}(\theta) - 4Pq_c^2]\sigma^2 + [4\epsilon q_c^2 P \widetilde{G}(\theta)
$$

$$
- 4P^2 q_c^4 \sin^2\theta]\sigma + \epsilon \left[\widetilde{G}(\theta) 4P^2 q_c^4 \sin^2\theta \right.
$$

$$
\left. + 4p P q_c^2 \left(v_1(\theta)\cos^2\frac{\theta}{2} + v_2(\theta)\sin^2\frac{\theta}{2} \right) \right] = 0. \quad (2.44)
$$

Figure 1 displays, for various values of the Prandtl number, and various rotation rates and distances from threshold, the growth rate of the unstable mode as obtained from the above model (solid line), and as derived in Ref. [6] from the primitive equations (dashed lines). An excellent agreement is obtained throughout the range of perturbation angles. Note that

the present model directly exhibits the ''small-angle instability'' derived in Ref. [6] from the primitive equations using matched asymptotic expansions. The effect on the nonlinear dynamics of this instability which results from the presence of an intense mean flow at small θ and which exists for arbitrary small rotation is discussed in Sec. IV.

C. A simplified model

The model considered in Sec. II B correctly reproduces the destabilization of convective rolls in rotating convection, but is relatively cumbersome. It is thus desirable to simplify it heuristically, in a way which preserves quantitatively its most prominent features. In this section, we also extend the model to the case of no-slip top and bottom boundaries. In the latter case, we systematically derive all the linear terms and also the nonlinear terms entering the mean flow equation, but resort to modeling the nonlinear couplings arising in the equation for the convective mode w.

Assuming that the field w can be viewed as a superposition of straight rolls with different wave vectors, the nonlinear term $\mathcal{N}$ vanishes and $\Delta_h \mathcal{M} = 4\mathcal{H}$. This leads to replacing Eqs. (2.37)–(2.40) by

$$
(\Delta_h - 4\pi^2)^2 w_2 - 4\pi r_0 \Delta_h \psi_2 + \Delta_h \theta_2 = \frac{3}{2}\frac{\pi}{q_c^2 P} \Delta_h \mathcal{M},
$$
$$
\quad (2.45)
$$

$$
4\pi r_0 w_2 - (\Delta_h - 4\pi^2)\Delta_h \psi_2 = 0, \quad (2.46)
$$

$$
R_c w_2 + (\Delta_h - 4\pi^2)\theta_2 = \frac{3}{2}\frac{\pi}{q_c^2}q_p^2 \mathcal{M}. \quad (2.47)
$$

Applying the operators $(\Delta_h - 4\pi^2)$ to Eq. (2.45), $-4\pi r_0 \Delta$ to Eq. (2.46) and $-\Delta_h$ to Eq. (2.47), and combining the resulting equations, we obtain

$$
[(\Delta_h - 4\pi^2)^3 - (4\pi r_0)^2 - R_c \Delta_h]w_2
$$

$$
= -\frac{3}{2}\pi \frac{q_p^2}{q_c^2}\Delta_h \mathcal{M} + \frac{3}{2}\frac{\pi}{q_c^2 P}(\Delta_h - 4\pi^2)\Delta_h \mathcal{M}. \quad (2.48)
$$

The action of the horizontal Laplacian Δ_h on straight rolls reduces to multiplication by $-q_c^2$. For rotations sufficiently slow to keep q_c small enough compared to 2π, we replace $(\Delta_h - 4\pi^2)$ by $-4\pi^2$, an approximation also used in Ref. [17]. Note that, although often neglected, nonlocal effects may in some instance be relevant, as stressed in Ref. [18].

Performing this localization as a first step, Eqs. (2.45)–(2.47) become

$$
-[(4\pi^2)^3 + (4\pi r_0)^2]w_2 = -\pi\left[\frac{3}{2}\frac{q_p^2}{q_c^2}\left(1 + \frac{4\pi^2}{q_p^2 P}\right)\right]\Delta_h \mathcal{M}
$$
$$
\quad (2.49)
$$

and

$$w_2 = \pi\lambda\Delta_h\mathcal{M}, \qquad (2.50)$$

$$\phi_2 = -2\pi^2\lambda\mathcal{M}, \qquad (2.51)$$

$$\theta_2 = -\kappa\mathcal{M}, \qquad (2.52)$$

$$\psi_2 = -r_0\lambda\mathcal{M}, \qquad (2.53)$$

with

$$\lambda = \frac{3}{2}\frac{q_p^2}{q_c^2}\frac{\left(1+\dfrac{4\pi^2}{q_p^2 P}\right)}{[(4\pi^2)^3+(4\pi r_0)^2]}, \quad \kappa = \frac{3q_p^2}{8\pi q_c^2}. \quad (2.54)$$

Rescaling the spatial variables by q_c, the time by q_c^2, defining $W = w(g\pi\kappa q_c^4/q_c^2\xi_0)^{1/2}$ and $\Psi = \psi_0 q_c^2(g\pi\kappa q_c^4/q_c^4\xi_0)$, and dropping the subscript h in the horizontal derivatives, we obtain

$$\tilde{\tau}_0\partial_t W = [\tilde{\epsilon}-(\Delta+1)]^2]W - \mathcal{N}_l(W,\mathcal{M},\Psi), \quad (2.55)$$

$$(\partial_t - P\Delta)\Delta\Psi = \frac{\pi^2}{2q_c^2}\left[1-\left(\frac{\tau}{q_p^2}\right)^2\right](\nabla\Delta W\times\nabla W)\cdot\hat{\mathbf{z}},$$

$$-\frac{\tau\pi^2}{q_p^2 q_c^2}[(\Delta W)^2+\nabla W\cdot\nabla\Delta W], \qquad (2.56)$$

where $\tilde{\tau}_0 = (1+(1/P)[1-(2\tau^2\pi^2/R_c q_c^2)])$, $\tilde{\epsilon} = \epsilon/q_c^4\xi_0$, and $\mathcal{M} = W^2 + (\nabla W)^2$.

The nonlinear coupling $\mathcal{N}_l$, resulting from the localization of Eq. (2.23), is a complicated expression which, in the infinite Prandtl number limit, reduces to

$$\mathcal{N}_l^\infty = -\Delta\left[w\mathcal{M}+\alpha w\Delta\mathcal{M}-(\tfrac{1}{2}-2\alpha)\nabla w\cdot\nabla\mathcal{M}\right.$$

$$\left.+\frac{\tau}{2}\delta(\nabla w\times\nabla\mathcal{M})\cdot\hat{\mathbf{z}}\right] \qquad (2.57)$$

with $\alpha = 6q_p^2/[(4\pi^2)^3+(2\pi\tau)^2]$ and $\delta = (1/q_p^2)[1+(6q_p^4 q_c^2/[(4\pi^2)^3+(2\pi\tau)^2])]$. In this limit, the model is similar to that of Refs. [10] and [11]. In particular, the coefficient δ identifies with that arising in Eq. (75) of Ref. [10], and the growth rate of the Küppers-Lortz instability is identical in both models. When the Prandtl number is decreased, this growth rate deviates significantly from that obtained with the primitive Boussinesq equations. The localization procedure thus appears to be inadequate for rotating convection at a small Prandtl number, and we resort to heuristically modifying the nonlinear couplings resulting from the localization in a way which both simplifies their expressions and improves the description of the Küppers-Lortz and small-angle instabilities. For this purpose, we select a few representative nonlinear terms originating from $\mathcal{N}_l$, retaining (with modified coefficients) the terms present at the infinite Prandtl number, except the term proportional to $W\Delta\mathcal{M}$ since its contribution in the linear analysis is similar to that originating from $\nabla w\cdot\nabla\mathcal{M}$. Among the terms involving the stream function Ψ, we retain the advection term

$(\nabla W\times\nabla\Psi)\cdot\hat{\mathbf{z}}$ and two additional terms, $W\Delta\Psi$ and $\nabla W\cdot\nabla\Delta\Psi$, which appear to be necessary in order to reproduce the Küppers-Lortz instability growth rate accurately. We also remove the outer Laplacian which does not affect the Küppers-Lortz stability. The effect of this operator is, however, significant far enough from onset where it contributes to distort the Busse balloon in a way similar to the nonvariational terms added by Cross and Greenside [19]. The equation for the mean flow is kept unchanged. We finally obtain the simplified system

$$\tilde{\tau}_0\partial_t W = [\tilde{\epsilon}-(\Delta+1)^2]W - \mathcal{N}_l(W,\Psi), \qquad (2.58)$$

$$(\partial_t - P\Delta)\Delta\Psi = \alpha_0(\nabla\Delta W\times\nabla W)\cdot\hat{\mathbf{z}}$$

$$+\alpha_6[(\Delta W)^2+\nabla W\cdot\nabla\Delta W], \quad (2.59)$$

where $\mathcal{N}_l$ is now given by

$$\mathcal{N}_l(W,\Psi) = \mathcal{M}W+\alpha_1\nabla W\cdot\nabla\mathcal{M}+\alpha_2(\nabla W\times\nabla\mathcal{M})\cdot\hat{\mathbf{z}}$$

$$+\alpha_3(\nabla W\times\nabla\Psi)\cdot\hat{\mathbf{z}}+\alpha_4 W\Delta\Psi+\alpha_5\nabla W\cdot\nabla\Delta\Psi. \qquad (2.60)$$

In this system,

$$\tilde{\tau}_0 = 1+\frac{1}{P}\left(1-\frac{2\tau^2\pi^2}{R_c q_c^2}\right), \qquad (2.61)$$

$$\tilde{\epsilon} = \frac{\epsilon}{q_c^4\xi_0}, \qquad (2.62)$$

$$\alpha_0 = \frac{\pi^2}{2q_c^2}(1-\beta^2), \qquad (2.63)$$

$$\alpha_3 = 8\tilde{\tau}_0, \qquad (2.64)$$

$$\alpha_4 = -\frac{8}{P}\frac{\pi^2}{q_c^2}\beta, \qquad (2.65)$$

$$\alpha_5 = \frac{16}{3P}\frac{\pi^2}{q_c^2}\beta, \qquad (2.66)$$

$$\alpha_6 = -\frac{\pi^2}{q_c^2}\beta, \qquad (2.67)$$

with $\beta = \tau/q_p^2$. The values of α_0, α_3, and α_6 result directly from the localization procedure. In contrast, the coefficients α_1 and α_2, are prescribed by fitting with the asymptotic model derived in Sec. II A. Indeed, a stability analysis similar to that leading to Eqs. (2.42) and (2.43), gives, in the present context
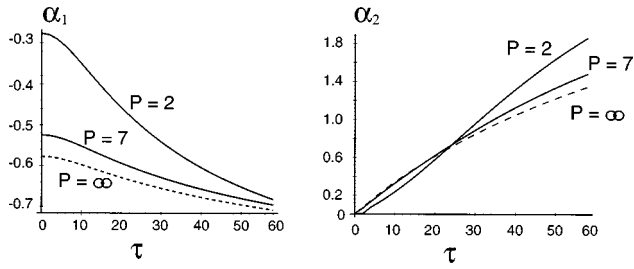
FIG. 2. Variation with the rotation rate of the coefficients α_1 and α_2 entering Eq. (2.60) of the simplified model for free-slip boundary conditions and different values of the Prandtl number.

$$\partial_t \begin{bmatrix} b \\ z_1 \\ z_2 \end{bmatrix} = \begin{bmatrix} \widetilde{\epsilon} g(\theta) & v_1(\theta) & v_2(\theta) \\ \widetilde{\epsilon} p & -4P\sin^2\frac{\theta}{2} & 0 \\ \widetilde{\epsilon} p & 0 & -4P\cos^2\frac{\theta}{2} \end{bmatrix} \begin{bmatrix} b \\ z_1 \\ z_2 \end{bmatrix},$$

(2.68)

with

$$g(\theta) = \frac{1}{\widetilde{\tau_0}} \left(1 - \frac{8 + 4\alpha_1 \sin^2\theta - 2\alpha_2 \sin 2\theta}{4 + \frac{\alpha_6}{8}P(4\alpha_4 + 8\alpha_5)} \right)$$
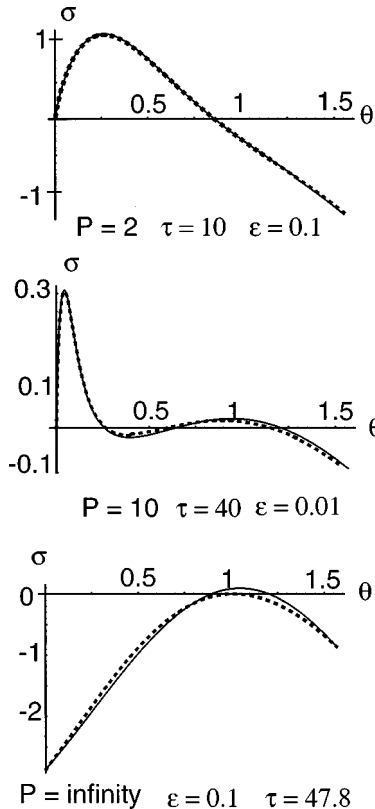
FIG. 3. Growth rates of the small-angle and Küppers-Lortz instabilities obtained from the primitive equations (dashed line) and the simplified model (2.58)–(2.60) (solid line) for different values of P, τ, and ϵ in the case of free-slip boundary conditions.

$$v_1(\theta) = \frac{1}{\widetilde{\tau_0}} \left(\alpha_3 \sin\theta + 4\alpha_4 \sin^2\frac{\theta}{2} + 8\alpha_5 \sin^4\frac{\theta}{2} \right),$$

$$v_2(\theta) = \frac{1}{\widetilde{\tau_0}} \left(-\alpha_3 \sin\theta + 4\alpha_4 \cos^2\frac{\theta}{2} + 8\alpha_5 \cos^4\frac{\theta}{2} \right),$$

$$p = -\frac{\alpha_6}{4 + \frac{\alpha_6}{8P}(4\alpha_4 + 8\alpha_5)}. \tag{2.69}$$

The coefficients α_1 and α_2 are prescribed by minimizing $|G(\theta) - g(\theta)|^2$ by a mean-square method. The variation of the resulting coefficients with the rotation rate is illustrated for various Prandtl numbers in Fig. 2.

In order to test the validity of the above determination, in Fig. 3 we compare the growth rate obtained in Sec. II B with that resulting from the primitive equation [6]. The fit is very accurate in the range of moderate Prandtl numbers we are mostly interested in here, but slightly deteriorates at infinite Prandtl number where the critical rotation rate given by the simplified model is $\tau_c = 45$ instead of $\tau_c = 47.8$. Simulations in the nonlinear regime also provide satisfactory agreement concerning the pattern formation between simplified and asymptotic models. Note that a further simplification such as that corresponding to the model of Ref. [14] leads to a significant loss of accuracy in the estimate of the critical rotation for the Küppers-Lortz instability.

D. Modeling rigid boundaries

It is customary, in the context of Swift-Hohenberg-type equations, to model the effect of rigid boundaries by adding a term in the mean flow equation which takes into account the friction of the mean flow on the top and bottom plates. Indeed, while with free-slip boundaries the mean flow is to leading order independent of the vertical coordinate, in the case of rigid boundaries it is to a good approximation a Poiseuille-type flow whose stream function can be modeled by $\Psi(x,y)\sin\pi z$. Projecting Eq. (2.6) on this mode, the operator $\partial_t - P\Delta$, when acting on $\Psi(x,y)$, reads $\partial_t - P(\Delta_h + \pi^2)$, which after normalization leads to replacing the left-hand side of Eq. (2.59) (where the subscript h has been dropped by $[\partial_t - P(\Delta_h + \nu)]\Delta_h$, with $\nu = \pi^2/q_c^2$. The value $\nu = 2$, used in the literature [20], can be understood if one keeps $q_c = \pi/\sqrt{2}$, even in the case of rigid boundaries. In the presence of rotation, the effect of top and bottom rigid boundaries is in fact more subtle, and this led us to derive, in a more systematic way, appropriate equations for this case.

Proceeding as in Ref. [13], we expand the temperature on the set of functions $\sin(2\pi n z)$ [in order to satisfy the boundary conditions $\theta(0) = \theta(1) = 0$], and use the eigenmodes of the operator d^4/dz^4, which vanish together with their first derivatives on $z = 0$ and 1, to expand the vertical velocity w. To leading order, we take $w = w_1 g(\pi z)$, where

$$g(z) = \frac{\cosh\lambda_1\left(\frac{z}{\pi} - \frac{1}{2}\right)}{\cosh\lambda_1/2} - \frac{\cos\lambda_1\left(\frac{z}{\pi} - \frac{1}{2}\right)}{\cos\lambda_1/2}, \quad (2.70)$$

with $\lambda_1 \approx 4.730\,040\,74$. Note that $\langle g(\pi z)^2\rangle \equiv \int_0^1 g^2(\pi z)dz = 1$. We also project ϕ and ψ on $g'(\pi z)$ and ψ_0 on $\sin\pi z$.

In the following, we systematically derive the linear part of the generalized Swift-Hohenberg system for rigid boundaries, and model the nonlinear terms in the spirit of the couplings obtained with free-slip boundaries. We proceed as in Sec. II assuming the amplitude of w_1 to be of order $\epsilon^{1/2}$, the time derivative of order ϵ, with a Rayleigh number $R = (1+\epsilon)R_c$. We also write the horizontal Laplacian $\Delta_h = -q_c^2 + \mathcal{L}$. Since the nonlinear terms in the Boussinesq equations arise only at order $\epsilon^{3/2}$, we restrict ourselves to the linear terms. Projecting Eq. (2.7) onto $g(\pi z)$, Eq. (2.6) onto $g'(\pi z)$, and Eq. (2.3) onto $\sin(\pi z)$, we obtain

$$P^{-1}\partial_t(\Delta_h - g_1\pi^2)w_1 = (\Delta_h - 2\pi^2\Delta_h g_1 + \pi^4 g_4)w_1 + g_s\Delta_h\theta_1$$
$$- \pi\tau g_1\Delta_h\psi_1, \quad (2.71)$$

$$\partial_t - P(\Delta_h - g_2\pi^2)\Delta_h\psi_1 = -\tau P\pi w_1, \quad (2.72)$$

$$\partial_t\theta_1 - (\Delta_h - \pi^2)\theta_1 = 2Rg_sw_1, \quad (2.73)$$

with $g_1 = \langle g'(\pi z)^2\rangle$, $g_2 = \langle g''(\pi z)^2\rangle/\langle g'(\pi z)^2\rangle$, $g_4 = \langle g(\pi z)g^{(4)}(\pi z)\rangle$, and $g_s = \langle g(\pi z)\sin(\pi z)\rangle$.

Applying the operators $(\Delta_h - g_2\pi^2)[\partial_t - (\Delta_h - \pi^2)]$ onto Eq. (2.71), $(\Delta_h - g_2\pi^2)g_s\Delta_h$ onto Eq. (2.73), and $P^{-1}\tau\pi g_1(\Delta_h - \pi^2)$ onto Eq. (2.72), and summing the resulting equations, we obtain, at leading order, the critical Rayleigh number

$$R_c = \frac{q_p^2(q_c^4 + 2\pi^2 q_c^2 g_1 + \pi^4 g_4)}{2g_s^2 q_c^2} + \frac{q_p^2\pi^2\tau^2 g_1}{2g_s^2 q_c^2 q_{p2}^2}, \quad (2.74)$$

with $q_p^2 = q_c^2 + \pi^2$ and $q_{pi}^2 = q_c^2 + g_i\pi^2$, the critical wave number q_c being given by the condition $\partial R_c(q_c)/\partial q = 0$ which arises at the order ϵ of the expansion.

At order $\epsilon^{3/2}$, the nonlinear terms are relevant but, as already mentioned, they will be specified phenomenologically. The linear part of the equation for the convective mode reads

$$\tau_0\partial_t w_1 = \epsilon w_1 - \xi_0\mathcal{L}^2 w_1, \quad (2.75)$$

where

$$\tau_0 = \frac{1}{q_p^2}\left[1 + P^{-1}\left(\frac{q_p^4 q_{p1}^2}{2R_c g_s^2 q_c^2} - \frac{q_p^4 g_1\pi^2\tau^2}{2R_c g_s^2 q_{p2}^4 q_c^2}\right)\right] \quad (2.76)$$

and

$$\xi_0 = \frac{2q_{p1}^2 + q_p^2}{2R_c g_s^2 q_c^2} - \frac{g_1\pi^2\tau^2}{2g_s^2 q_c^2 R_c q_{p2}^2}\left(1 - \frac{q_p^2}{q_{p2}^2}\right). \quad (2.77)$$

In the absence of rotation, we thus have $\tau_0 = (1 + 0.5143P^{-1})/19.46$, to be compared with the value $\tau_0 = (1 + 0.5117P^{-1})/19.65$ obtained using a projection on three Galerkin modes [21]. Similarly, we obtain for

$\bar{\xi}_0^2 = 4q_c^2\xi_0$ (a quantity usually denoted ξ_0^2 in the literature) the value 0.151 instead of 0.148. The leading order of the vertical vorticity equation (2.72) gives $\psi_1 = (\pi/q_c^2)\beta w_1$ where $\beta = \tau/q_{p2}^2$, and the incompressibility condition implies $\phi_1 = (\pi/q_c^2)w_1$. We thus write

$$\mathbf{V} = \begin{bmatrix} \dfrac{\pi^2}{q_c^2}(\partial_x + \beta\partial_y)w_1 g'(\pi z) + \partial_y\psi_1\sin(\pi z) \\[2mm] \dfrac{\pi^2}{q_c^2}(\partial_y - \beta\partial_x)w_1 g'(\pi z) - \partial_x\psi_1\sin(\pi z) \\[2mm] w_1 g(\pi z) \end{bmatrix}. \quad (2.78)$$

Using Eq. (2.78) in the next order contribution to the equation for the vertical vorticity, projecting on the $\sin(\pi z)$ mode and rescaling the dependent and independent variables as in the free-slip case, we obtain

$$[\partial_t - P(\Delta - \nu)]\Delta\Psi = \alpha_0(\nabla_h\Delta W\times\nabla W) + \alpha_6[(\Delta W)^2$$
$$+ \nabla W\cdot\nabla\Delta W] + \alpha_7\Delta(W^2), \quad (2.79)$$

where

$$\alpha_0 = 4\langle g'^2(\pi z)\sin(\pi z)\rangle\frac{\pi^2}{2q_c^2}(1 - \beta^2), \quad (2.80)$$

$$\alpha_6 = -4\langle g^2(\pi z)\sin(\pi z)\rangle\frac{\beta\pi^2}{q_c^2}, \quad (2.81)$$

$$\alpha_7 = -\langle[g''(\pi z)g(\pi z) + g'^2(\pi z)]\sin(\pi z)\rangle\frac{\beta\pi^2}{q_c^2}, \quad (2.82)$$

$$\nu = \frac{\pi^2}{q_c^2}. \quad (2.83)$$

It is noticeable that, when compared to its analog in the case of free-slip boundaries, Eq. (2.79) includes an additional term proportional to $\Delta(W^2)$ originating from the vertical Reynolds stress.

Returning to the equation for the vertical velocity, we model the nonlinear couplings as in the case of free-slip boundaries. Neglecting the last two terms on the right-hand side of Eq. (2.59) which are used to refine the stability analysis of straight parallel rolls in the case of free-slip boundary conditions, we find

$$\tilde{\tau}_0\partial_t W = [\tilde{\epsilon} - (\Delta + 1)^2]W - [W\mathcal{M} + \alpha_1\nabla W\cdot\nabla\mathcal{M} + \alpha_2\nabla W$$
$$\times\nabla\mathcal{M} + \alpha_3\nabla W\times\nabla\Psi], \quad (2.84)$$

with

$$\tilde{\tau}_0 = \frac{\tau_0 q_c^2}{q_c^4\xi_0}, \quad \tilde{\epsilon} = \frac{\epsilon}{q_c^4\xi_0}. \quad (2.85)$$

TABLE I. Values of the coefficients γ_1, γ_2, and γ_3 entering the model with rigid boundary conditions (see text) for various values of the Prandtl number, together with characteristics of the KL and zigzag instabilities.

P	θ_{KL}	τ_{KL}	$(\widetilde{\epsilon}_{zigzag}, k_{zigzag})$	γ_1	γ_2	γ_3
0.8	38.4°	23.6	(0.232, 0.866)	−0.010	0.049 04	1.4187
1.2	46°	29.6	(0.232, 0.875)	0.0106	0.020 05	2.1644
2	50°	38	(0.4708, 0.847)	0.0112	0.020 77	2.3076
6.8	59.1°	46.2	(0.4754, 0.8502)	0.0147	0.007 59	8.809
50	59.7°	54.8	(0.8, 0.9778)	0.0120	0.020 02	5.0
∞	59.7°	54.8		0.0120	0.021 32	0

The coefficients α_1, α_2, and α_3 are prescribed as follows. As in the case of free-slip boundaries, we take $\alpha_3 = \gamma_3 \widetilde{\tau}_0$, with a coefficient γ_3 to be determined. Similarly, we take $\alpha_2 = \gamma_2 \widetilde{\tau}_0$, since, in the free-slip case, the variation of α_2 with the rotation rate is almost linear. Finally, we choose $\alpha_1 = -\gamma_1 \widetilde{\tau}_0$ since the corresponding term disappears in the absence of rotation. The coefficients γ_1, γ_2, and γ_3 are determined in such a way as to recover accurately the Küppers-Lortz instability for moderate Prandtl numbers and the zigzag instability boundary in the absence of rotation. The latter constraint is met by comparing the predictions of the phase equation analysis made in Sec. III [see Eq. (3.19)], with that performed on the primitive Boussinesq equations with rigid boundary conditions [22]. Note that an accurate description of the right-hand boundary of the Busse balloon (skewed-varicose instability) requires the inclusion of nonvariational additional terms [19]. In the neighborhood of the threshold (whose extension increases with the Prandtl number), the present model provides an adequate representation of the long-wavelength instabilities.

In practice, the model has been considered for different values of the Prandtl number for which the onset of the Küppers-Lortz instability is computed in Refs. [4] or [5]. This leads to the numerical values of the coefficients γ_1, γ_2, and γ_3 given in Table I.

III. WEAKLY NONLINEAR DYNAMICS

A. Nonlinear development of the small-angle instability

At a finite Prandtl number and moderate rotation, the development of the small-angle instability is visualized by solving the model equations (2.58)–(2.60), starting with
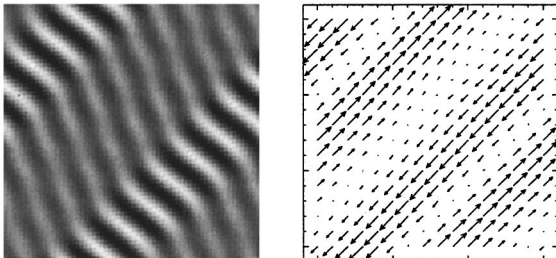

FIG. 4. Weakly nonlinear dynamics resulting from the small-angle instability for $P=2$, $\tau=10$, and $\widetilde{\epsilon}=0.1$: (a) convection rolls; (b) mean flow stream function.

straight parallel rolls of the critical wave number, perturbed by a small isotopic noise. Under the effect of the small-angle instability, the rolls distort and shear layers are formed, as seen in Fig. 4. The reconnection of the rolls leads to a global rotation of the pattern in the direction of the external rotation. Indeed, the vorticity generated by the last term on the right-hand side of Eq. (2.59) has, preferentially, the sign of the external rotation. This process is easily seen in Fourier space, where the leading mode rotates on the critical circle.

B. Derivation of the phase-mean drift equations

In order to describe the phase modulation of straight parallel rolls, we proceed as in Ref. [23], and introduce the slow variables $\vec{X} = \eta \vec{x}$ and $T = \eta^2 t$. We also denote the phase variable by θ, the slow phase by $\Theta = \eta^{-1}\theta$, and the local wave vector by $\vec{K} = \nabla_X \Theta$. We are thus led to replace, in the models with free slip [Eqs. (2.58) and (2.59)] or rigid [Eqs. (2.84) and (2.79)] boundary conditions, the time derivative ∂_t by $\eta \partial_T \Theta \partial_\theta + \eta^2 \partial_T$, the gradient ∇ with respect to $\vec{X}$ by $\vec{K}\partial_\theta + \eta \nabla$, and the Laplacian ∇^2 by $K^2 \partial_\theta^2 + \eta D_1 \partial_\theta + \eta^2 \nabla^2$ with $D_1 = 2\vec{K}\cdot\nabla + \nabla\cdot\vec{K}$. We expand the solution $\mathcal{S} = \binom{W}{\Psi}$ as

$$\mathcal{S} = \mathcal{S}_0 + \eta \mathcal{S}_1 + \cdots = \begin{pmatrix} w_0 + \eta w_1 + \cdots \\ \psi_0 + \zeta_0 + \eta(\psi_1 + \zeta_1) + \cdots \end{pmatrix}, \quad (3.1)$$

where the contributions depending on the fast phase θ are isolated in the quantities ζ_i.

At leading order, we have

$$\mathcal{L}_0 S_0 \equiv \begin{pmatrix} \hat{O}_{11} & \hat{O}_{12} \\ \hat{O}_{21} & \hat{O}_{22} \end{pmatrix} = 0, \quad (3.2)$$

where

$$\hat{O}_{11} = [-\epsilon + (K^2\partial_\theta^2 + 1)^2]w_0 + \{w_0^3 + w_0(\partial_\theta w_0 \vec{K})^2$$
$$+ \alpha_1[K^2\partial_\theta w_0 \partial_\theta(w_0^2) + K^4\partial_\theta w_0 \partial_\theta(\partial_\theta w_0)^2]$$
$$+ \alpha_4(w_0 K^2\partial_\theta^2\psi_0) + \alpha_5(K^4\partial_\theta w_0\partial_\theta^3\psi_0)\}, \quad (3.3)$$

$$\hat{O}_{12} = \alpha_4(w_0 K^2\partial_\theta^2\psi_0) - \alpha_5(K^4\partial_\theta w_0\partial_\theta^3\psi_0), \quad (3.4)$$

$$\hat{O}_{21} = P(-K^2\partial_\theta^2 + \nu)\partial_\theta^2\psi_0, \quad (3.5)$$

$$\hat{O}_{22} = -\alpha_6[K^4\partial_\theta w_0\partial_\theta^3 w_0 + K^4(\partial_\theta^2 w_0)^2] - \alpha_7 K^2\partial_\theta^2 w_0^2. \quad (3.6)$$

Retaining only the first mode in a Galerkin expansion, we write the solution in the form $(w_0 = A\cos\theta, \psi_0 = A^2\phi\cos2\theta)$, with $\phi = -(\alpha_6 K^2 - 2\alpha_7)/4P(\nu + 4K^2)$ and

$$A^2 = \frac{\widetilde{\epsilon} - (K^2 - 1)^2}{\dfrac{3}{4} + \dfrac{K^2}{4} + \dfrac{1}{2}\alpha_1 K^2(1 - K^2) - 2K^2\phi(\alpha_4 + 2K^2\alpha_5)}. \quad (3.7)$$

The evolution of ζ_0 is determined at the next order of the expansion.

At order η, the equation takes the form

$$\delta\mathcal{L}_0 \mathcal{S}_1 = \mathcal{F}_1, \qquad (3.8)$$

where $\delta\mathcal{L}_0$ is the linearization of the operator $\mathcal{L}_0$ about the steady solution, and $\mathcal{F}_1$ collects the terms of order η not involving $\mathcal{S}_1$. The solvability conditions are obtained by taking the scalar product $\langle a,b \rangle = (1/2\pi)\int_0^{2\pi} ab\, d\theta$ from the right-hand side of Eq. (3.8) with the vectors which span the null space of the adjoint $\delta\mathcal{L}_0^\dagger$ of the operator $\mathcal{L}_0$, namely, $e_1 = (\sin\theta, \gamma\sin 2\theta)$ where $\gamma = -A(\alpha_4 + 2\alpha_5 K^2)/[2P(\nu + 4K^2)]$, and $e_2 = (0,1)$. The first solvability condition gives the phase diffusion equation

$$\tau(K)\partial_T\Theta + g(K)\vec{K}\times\nabla\zeta_0 + a(K)(\vec{K}\cdot\nabla)K^2$$
$$+ b(K)(\vec{K}\times\nabla)K^2 + c(K)\nabla\cdot\vec{K} = 0, \qquad (3.9)$$

with

$$\tau(K) = \tfrac{1}{2}\tau_0 A^2 - 4\gamma K^2 A^3 \phi, \qquad (3.10)$$

$$g(K) = \tfrac{1}{2}\alpha_3 A^2, \qquad (3.11)$$

$$a(K) = -A^2 + (1-K^2)\frac{dA^2}{d(K^2)} + \frac{1}{8}A^2\frac{dA^2}{d(K^2)}$$
$$+ \alpha_1\left(\frac{1}{4}(1+2K^2)A^2\frac{dA^2}{d(K^2)} + \frac{3}{8}A^4\right)$$
$$+ \alpha_4 A^2\frac{d(A^2\phi)}{d(K^2)} + \alpha_5\left[2K^2A^2\frac{d(A^2\phi)}{d(K^2)} + A^4\left(\phi\right.\right.$$
$$\left.\left. + K^2\frac{d\phi}{d(K^2)}\right)\right] + \gamma\left[8PA^3\left(\phi + K^2\phi\frac{dA^2}{d(K^2)}\right.\right.$$
$$\left. + 2K^2\frac{d\phi}{d(K^2)}\right) + 2P(\nu+4k^2)\left(A\frac{d(\phi A^2)}{d(K^2)}\right)$$
$$\left. + \alpha_6\left(K^2A\frac{dA^2}{d(K^2)} + \frac{1}{4}A^3\right) - 2\alpha_7 A\frac{dA^2}{d(K^2)}\right], \qquad (3.12)$$

$$b(K) = -\alpha_2\left(\frac{1}{2}A^2K^2\frac{dA^2}{dK^2} + \frac{3}{8}A^4\right) - \frac{1}{4}\alpha_3 A^2\left(2\phi\frac{dA^2}{dK^2}\right.$$
$$\left. + A^2\frac{d\phi}{dK^2}\right) + \gamma\alpha_0\left(\frac{1}{8}A^2(K^2-1)\frac{dA^2}{dK^2} - \frac{1}{4}A^3\right), \qquad (3.13)$$

$$c(K) = (1-K^2)A^2 + \frac{1}{2}\alpha_4 A^2\phi + \alpha_5 K^2 A^2\phi$$
$$+ \gamma[P\phi A^3(\nu + 8K^2) + \frac{3}{4}\alpha_6 A^3 - \alpha_7 A^3]. \qquad (3.14)$$

The second solvability condition is always satisfied, and the expansion must thus be pushed to the next order.

At order η^2, we have an equation of the form

$$\delta\mathcal{L}_0 \mathcal{S}_2 = \mathcal{F}_2, \qquad (3.15)$$

and the solvability condition coming from the orthogonality of $\mathcal{F}_2$ with e_2 gives the mean flow equation

$$[\eta^2(\partial_T - P\nabla^2) + P\nu]\nabla^2\zeta_0$$
$$= \frac{\alpha_0}{2}\nabla\times[\vec{K}\nabla\cdot(\vec{K}A^2)] + \frac{\alpha_6}{2}\nabla\cdot[\vec{K}\nabla\cdot(\vec{K}A^2)] + \frac{\alpha_7}{2}\nabla^2 A^2, \qquad (3.16)$$

which, together with Eq. (3.9), provides the phase-mean drift system. To study the stability of the straight parallel rolls, we linearize Eqs. (3.9) and (3.16) about the solution $\Theta = kX$ and $\zeta_0 = 0$. The system for the perturbations φ and ξ of the phase and of the mean flow reads

$$\tau(k)\partial_T\varphi + g(k)\partial_Y\xi + 2a(k)k^2\partial_{XX}\varphi + 2b(k)k^2\partial_{XY}\varphi$$
$$+ c(k)\nabla^2\varphi = 0, \qquad (3.17)$$

$$[\eta^2(\partial_T - P\nabla^2) + P\nu]\nabla^2\xi$$
$$= -\frac{\alpha_0}{2}\left(kA(k)^2\partial_Y\nabla^2\varphi + 2k^3\frac{dA^2}{d(K^2)}(k)\partial_{XXY}\varphi\right)$$
$$+ \frac{\alpha_6}{2}\left(kA(k)^2\partial_X\nabla^2\varphi + 2k^3\frac{dA^2}{d(K^2)}(k)\partial_{XXX}\varphi\right)$$
$$+ \alpha_7 k\frac{dA^2}{d(K^2)}(k)\partial_X\nabla^2\varphi. \qquad (3.18)$$

Considering normal modes proportional to $e^{i\vec{\kappa}\cdot\vec{X}+\sigma T}$ with $\vec{\kappa} = (\kappa\cos\rho, \kappa\sin\rho)$, we obtain for the growth rate σ, a quadratic equation. One of the solutions is always negative. The other is given by

$$\frac{\sigma}{\kappa^2} = \frac{1}{2\tau(k)\eta^2}\left[-\tau(k)P(\eta^2+\nu) - \eta^2[2a(k)k^2\cos^2\rho\right.$$
$$+ b(k)k^2\sin 2\rho + c(k)] + \left\{\{\tau(k)P(\eta^2+\nu)\right.$$
$$+ \eta^2[2a(k)k^2\cos^2\rho + b(k)k^2\sin 2\rho + c(k)]\}^2$$
$$- 4\tau(k)\eta^2 g(k)(\alpha_0\sin^2\rho - \alpha_6\sin\rho\,\cos\rho)k\left(\frac{A(k)^2}{2}\right.$$
$$\left. + k^2\frac{dA^2}{d(K^2)}(k)\cos^2\rho\right) - 4\tau(k)\eta^2 g(k)$$
$$\left.\left. \times\left(-\alpha_7\sin\rho\cos\rho k\frac{dA^2}{d(K^2)}(k)\right)\right\}^{1/2}\right]. \qquad (3.19)$$

In Eq. (3.19), $\alpha_7 = \nu = 0$ in the case of free-slip boundary conditions while $\alpha_4 = \alpha_5 = 0$ for rigid boundary conditions.

C. Relation between the small-angle and skewed-varicose instabilities

In the absence of rotation and for free-slip boundaries, straight parallel rolls with a wave number larger than critical,
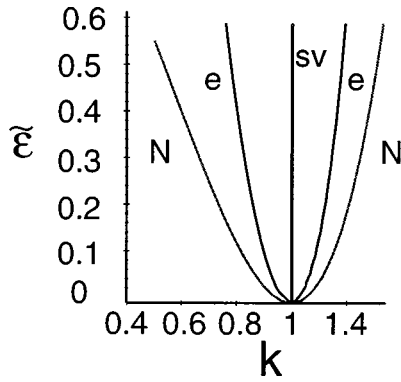
FIG. 5. Stability balloon relatively to long-wave instabilities in the case of free-slip boundary conditions for $P=2$ and $\eta=10^{-2}$, in the absence of rotation. Here, e represents the frontier of the Eckhaus instability and sv that of the skewed-varicose instability. Furthermore, N is the neutral curve for convection onset.

FIG. 7. Sketch in Fourier space of the couples of modes $e^{\pm i(\vec{k} \pm \eta \vec{\kappa}) \cdot \vec{x}}$ associated with the phase instability, for $k>q_c$ (a) and $k<q_c$ (b), together with the critical circle (of radius q_c).

were shown to be unstable with respect to the skewed-varicose instability [15,16]. This phenomenon is recovered by computing the stability balloon from Eq. (3.19). Taking the critical wave number q_c as unity, the result is illustrated in Fig. 5 for $P=2$ and $\eta=10^{-2}$. The dependency of the growth rate of the skewed-varicose instability with the angle ρ associated to the phase perturbation is presented in Fig. 6(a) for rolls of wave number $k=1.03$ and the same values of P and η as in Fig. 5. We note that, as usual, the growth rate is symmetric in terms of ρ.

When rotation is turned on, we observe that for $k>1$, the skewed-varicose instability becomes "asymmetric," the growth rate being now maximum for a finite value of the angle ρ whose sign is that of the rotation [Fig. 6(b)]. When k is smaller than critical, the unstable modes are associated to
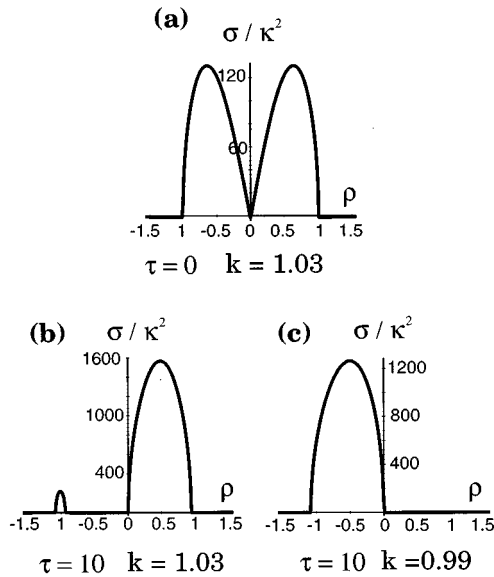
values of ρ, whose sign is opposite to that of the external rotation [Fig. 6(c)]. In physical space, a phase perturbation with an angle ρ produces a distortion of the rolls where compressed and dilated regions alternate along an axis making the same angle with k. The associated mean flow displays shear layers perpendicular to this axis. According to the angle ρ, the perturbation is amplified or not, as predicted by the phase modulation analysis. Note that the aspect ratio of the box required to validate the phase theory increases with the rotation rate.

It is of interest to compare more precisely the small-angle instability resulting from an amplitude perturbation with the asymmetric skewed-varicose instability associated with a phase perturbation. By inspection of Eq. (2.44), it is easily seen that, in the small-angle boundary layer, the growth rate of the amplitude perturbation scales like θ^2, where θ is the angle between the basic and the perturbation wave vectors, while Eq. (3.19) shows that the growth rate of the phase perturbation (in the primitive variables) scales like the inverse aspect ratio η of the box. On the other hand, in such a box, the minimum perturbation angle θ is of order $\eta^{1/2}$. It follows that both growth rates scale like the inverse aspect η and not like η^2, as usual for phase instabilities in the case of no-slip top and bottom boundaries. This larger growth rate results from the strong magnitude of the mean flow.

Furthermore, both instabilities lead to a similar dynamics in physical space, governed by the formation of shear layers which trigger the reconnection of the rolls and their global rotation. Nevertheless, the eigenmodes involved in the two descriptions of what appears to be essentially the same instability are different. In the amplitude framework, the perturbation consists of a single Fourier mode, which is always unstable if the angle of its wave vector, with that of the basic rolls, has the sign of the external rotation. In the phase formalism, in contrast, the perturbing modes can be viewed as a couple of satellites whose separation scales like the inverse aspect ratio η of the convection cell. In a confined system, the distance between the two satellites is sufficient to make the associated modes evolve as two independent amplitude perturbations. In contrast, when the aspect ratio of the box is large enough, the interaction of the two satellites is resonant, and a mode which alone would be unstable may be stabilized by the presence of its companion, as predicted by the phase theory. When the wave number is distinct from critical, the sign of the rotation can be predicted by noticing that among the two satellite modes produced by the phase perturbation, the closest to the critical circle will be preferentially amplified (Fig. 7). For example, for positive rotation and $k>q_c$,

FIG. 6. Growth rate σ/κ^2 relatively to long wave perturbations for $P=2$ and $\eta=10^{-2}$: (a) no rotation and basic rolls with wave number $k=1.03$, (b) rotation rate $\tau=10$ and roll wave number $k=1.03$ (in units of q_c); and (c) rotation rate $\tau=10$ and roll wave number $k=0.99$.
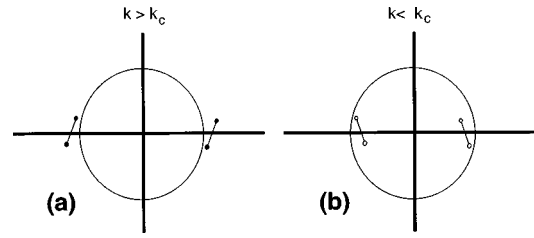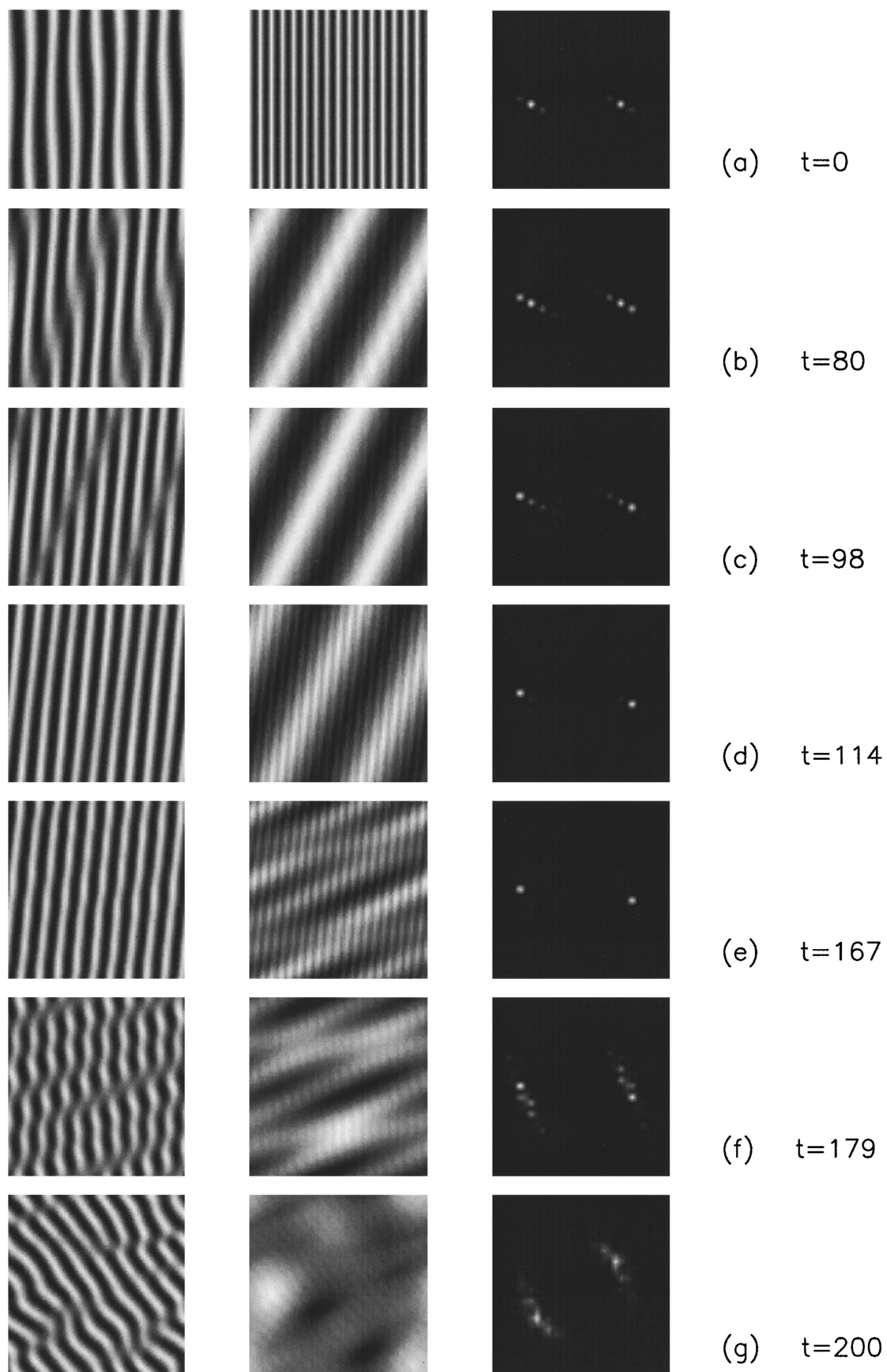
FIG. 8. Time evolution of parallel rolls with wave number $k = 0.9$ for $\widetilde{\epsilon} = 0.3$, and $\tau = 10$ subject to a phase perturbation: convective mode (left), mean flow stream function (middle), and two-dimensional energy spectrum of the convective mode (right).
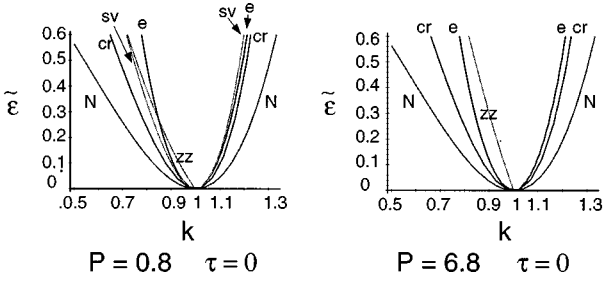
FIG. 9. Instability balloon for rigid boundary conditions in the absence of rotation for Prandtl numbers $P=0.8$ (a) and $P=6.8$ (b). Here e, sv, cr, and zz represent the frontiers of the Eckhaus, skewed-varicose, cross-roll and zigzag instabilities respectively. N is the neutral curve for the onset of convection.

the instability correspond to positive ρ [see Fig. 6(b)] and the rotation will be in the negative direction. Similarly, for $k < q_c$, modes with negative ρ are unstable [Fig. 6(c)] and the rotation also takes place in the negative direction. After a while, the mode close to the critical circle becomes dominant and the pattern undergoes a dynamics prescribed by the amplitude theory, possibly leading to the reversal of the rotation direction (Fig. 8).

D. Busse balloons for rigid boundary conditions

We first display in Fig. 9 the stability balloon in the absence of rotation for our model with rigid boundary conditions for $P=0.8$ and 6.8. Figure 10 displays the stability balloon for both Prandtl numbers in the presence of rotation. They qualitatively agree near threshold with those derived from the primitive equations [3]. Since our analysis is limited to a neighborhood of threshold, we did not include, as in Ref. [19], corrective terms designed to bend the balloon at higher values of ϵ. In this context, it is of interest to consider more precisely the effect of the rotation on the skewed-varicose instability, a question addressed experimentally in Ref. [9]. Tables II and III show for $P=0.8$ and $\widetilde{\epsilon}=0.3$ and 0.5, corresponding to two essentially constant values of the normalized distance ϵ to convection threshold, that the angle θ_{SV} of the wave-vector perturbation decays linearly as in the experimental results displayed in Fig. 18 of Ref. [9]. The growth of the critical wave number k_{SV} (see Fig. 2 of Ref. [9]) is, however, underestimated.

Figure 11 displays the stability border relative to long-wave instabilities in the plane (k, ρ). The symmetry (for
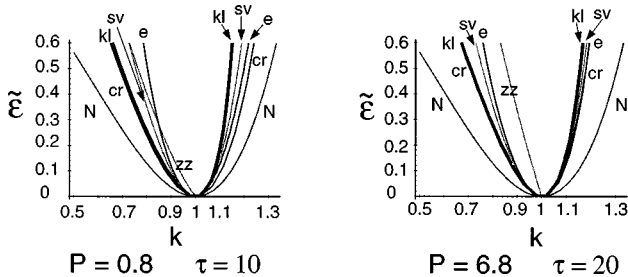

FIG. 10. Instability balloon in the presence of rotation ($\tau=20$) for rigid boundary conditions at Prandtl numbers $P=0.8$ and 6.8. The labels of the long-wave instability boundaries are those of Fig. 9, while kl refers to the Küppers-Lortz instability.

TABLE II. Variation of the critical wave number and of the angle of the skewed-varicose instability for $P=0.8$ and $\widetilde{\epsilon}=0.3$.

$\Omega = \tau/2$	k_{SV}	θ_{SV}	ϵ
0	1.138 67	46°	0.108
5	1.1402	41.8°	0.109
7	1.1411	40°	0.1097
10	1.143	37°	0.111
15	1.146 96	33.46°	0.1137

$\tau=0$) with respect to the phase perturbation angle ρ, which holds for $\tau=0$, is broken in the presence of rotation, as with free-slip boundary conditions.

IV. NONLINEAR DYNAMICS FOR FREE-SLIP BOUNDARY CONDITIONS

In order to simulate the fully nonlinear regime, Eqs. (2.58)–(2.60) were integrated with resolution ranging from 128^2 to 256^2 collocation points, according to the number of rolls in the convection cell. The initial conditions consist in a random noise with a spectrum localized in an annulus centered around the critical wave-number.

Typical snapshots of patterns emerging in the absence of rotation are displayed in Figs. 12 and 13. At an infinite Prandtl number, labyrinthic rolls [24] are observed (Fig. 12), while the now classical spiral turbulence state is obtained for a Prandtl number of order unity (Fig. 13).

The Küppers-Lortz instability regime which develops at an infinite Prandtl number and moderate rotation is shown in Fig. 14 for $\tau=50$ and $\epsilon=0.2$. We observe the formation of patches of parallel rolls of different orientations. As time elapses, each patch is gradually replaced by another one whose rolls are rotated by an angle close to $60°$, a dynamics similar to that described in Refs. [25] and [21]. The chaotic dynamics due to the KL instability is essentially governed by the propagation of dislocation arrays separating randomly oriented roll patches whose size is reduced as ϵ is increases.

Qualitatively different patterns are observed at smaller Prandtl numbers. This regime is illustrated in Fig. 15, which displays a snapshot of W and Ψ for $P=2$, $\tau=10$, and various values of the stress parameter ϵ. Near the onset ($\epsilon=0.01$), the pattern consists of large patches of slightly distorted parallel rolls [Fig. 15(a)], rotating slowly and reconnecting under the influence of the shear flow associated to the small-angle instability as discussed in Sec. III B. For $\epsilon=0.05$ [Fig. 15(b)], we observe after about ten horizontal diffusion times T_h, the emergence from the turbulent back-

TABLE III. Variation of the critical wave number and of the angle of the skewed-varicose instability for $P=0.8$ and $\widetilde{\epsilon}=0.5$.

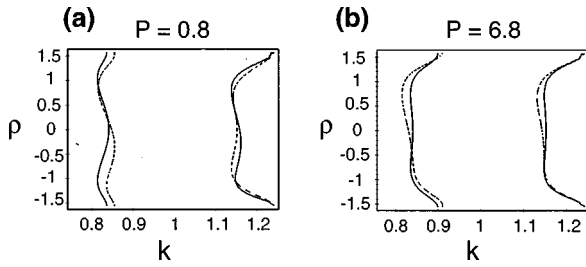| $\Omega = \tau/2$	k_{SV}	θ_{SV}	ϵ
0	1.1733	44.91°	0.1805
5	1.1759	40.68°	0.1817
7	1.1776	38.96°	0.1829
10	1.1806	36.66°	0.1851
15	1.1873	32.65°	0.1895

FIG. 11. Stability domain in the absence of rotation (solid line) and with a rotation rate $\tau=20$ (dashed line) in the (k,ρ) plane of the wave number and angle of phase perturbation, for the long-wave instabilities shown in Fig. 10, when $\widetilde{\epsilon}=0.3$, $\eta=10^{-2}$, and $P=0.8$ (a) or 6.8 (b).

FIG. 13. Convective pattern (left) and mean flow stream function (right) showing spiral turbulence in the case of free-slip boundary conditions, for $P=1$, $\epsilon=0.5$, and $\Gamma=32$, in the absence of rotation.

ground, of a big target associated to a coherent vortex, which survives for about 13 T_h and is then destroyed by a large-scale shear. Note that in presence of rotation, the mean flow survives at the center of a perfectly isotropic target, and that the targets rotate in the direction of the external rotation. For $\epsilon=0.2$, the target keeps growing by accretion of adjacent rolls until it reaches the size of the computational domain, and then stabilizes [Fig. 15(c)]. For an intermediate value of ϵ ($\epsilon=0.1$), the target does not stabilize, and a cyclic transition between a target and a spiral is observed (Fig. 16). When the rotation induces deformations, the innermost roll of the target meets its neighbor, and a pair of dislocations is formed. One of them glides inwards, forming a spiral, while the other is rapidly convected outwards by the mean flow, producing a whirling line of low amplitude. The target reforms when a dislocation of the opposite sign reaches the center of the spiral. For larger ϵ, the target rotates more rigidly, and becomes stable.

When analyzing the influence of the rotation rate, at fixed values of the Prandtl number ($P=2$) and of the stress parameter ($\widetilde{\epsilon}=0.05$), we notice that the structures formed at small rotation (e.g., $\tau=4$), are similar to those of Fig. 15(a), while for larger values of τ (e.g., $\tau=30$), the angular range of unstable modes becoming larger, the formation of coherent structures is prevented. More quantitatively, in Fig. 17, we consider for a Prandtl number $P=1.2$ and a stress parameter $\widetilde{\epsilon}=0.7$, the time variation of the correlation length
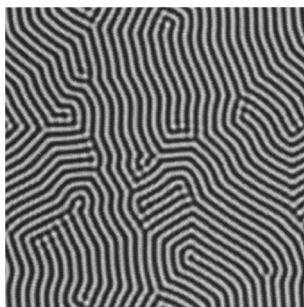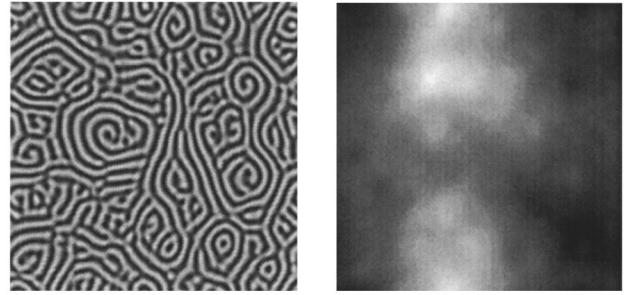
$$\zeta=\left(\frac{\int (k-\bar{k})^2|\hat{w}(k)|^2 d^2k}{\int |\hat{w}(k)|^2 d^2k}\right)^{-1/2}, \qquad (4.1)$$

where

$$\bar{k}=\frac{\int k|\hat{w}(k)|^2 d^2k}{\int |\hat{w}(k)|^2 d^2k}, \qquad (4.2)$$

We observe on Fig. 17(b) that when targets are formed the correlation increases and so does the mean flow, as measured by the squared L_2 norm $|\psi_0|_{L_2}$ of its stream function. The dynamics is also very sensitive to the Prandtl number. With the same value of the stress parameter $\widetilde{\epsilon}=0.7$ and the same rotation rate ($\tau=10$) but for a Prandtl number $P=10$, straight parallel rolls are obtained when the convection cell has an aspect ratio $\Gamma=16$, the small-angle instability being weak and the KL instability absent.

It is noticeable that the formation of stable targets is not specific to the case of periodic conditions in the horizontal directions. Such structures are also obtained in simulations performed in a cylindrical box with no-slip conditions on the side wall but free-slip top and bottom boundary conditions. In this case, the pattern adjusts to the symmetry of the container, leading to concentric rolls which occupy the whole
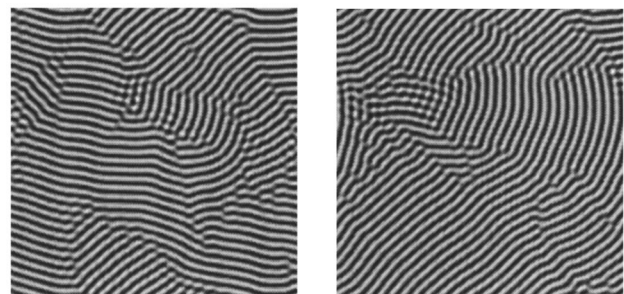

FIG. 12. Labyrinthic pattern at an infinite Prandtl number, for $\widetilde{\epsilon}=0.5$ and $\Gamma=32$, in the absence of rotation.

FIG. 14. Snapshots of the roll patch dynamics at an infinite Prandtl number for $\Gamma=32$, $\widetilde{\epsilon}=0.2$, and a rotation rate $\tau=50$.
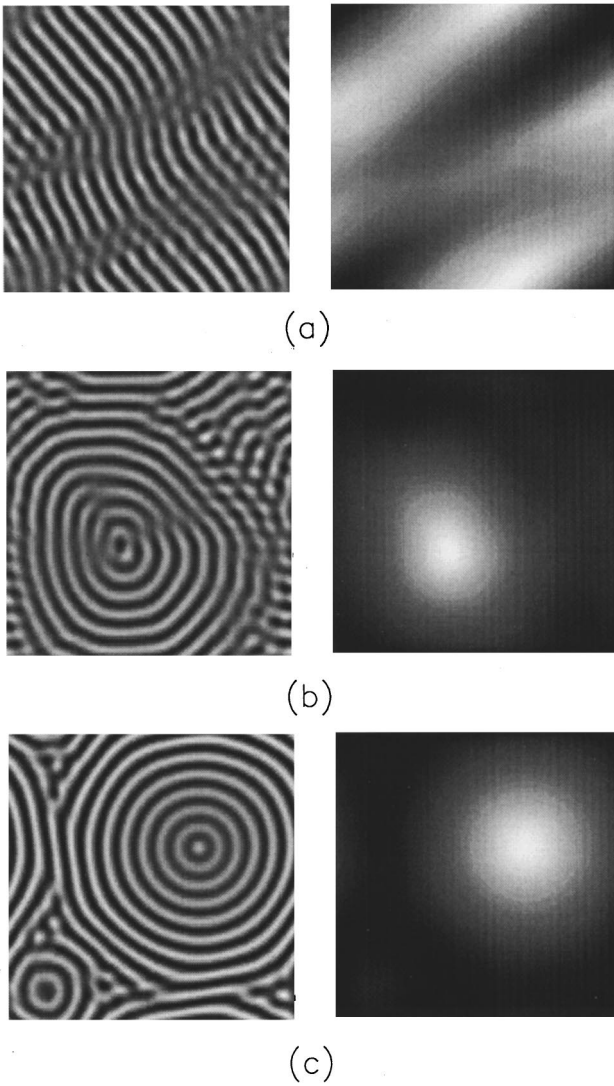
(a)

(b)

(c)

FIG. 15. Convective pattern (left) and mean flow stream function (right) for free-slip boundary conditions with $P = 2$, $\tau = 10$, $\Gamma = 16$, and increasing values of the stress parameter: $\widetilde{\epsilon} = 0.01$ (a), $\widetilde{\epsilon} = 0.05$ (b), and $\widetilde{\epsilon} = 0.2$ (c).

domain [26]. In contrast, as discuss in Sec. V, a different dynamics develop with rigid to and bottom boundary conditions where the small-angle instability does not exist.

V. NONLINEAR DYNAMICS FOR RIGID BOUNDARY CONDITIONS

The dynamics developing with rigid top and bottom boundaries and periodic conditions in the horizontal directions is displayed in Fig. 18, for a Prandtl number $P = 1.2$ and a stress parameter $\widetilde{\epsilon} = 0.7$. In the absence of rotation [Fig. 18(a)], we observe the now well-documented spiral turbulence [27–34]. The effect of a small rotation $\tau = 10$ [Fig. 18(b)] is to increase the size of the spirals and to force their rotating motion in the same direction as that of the external rotation [35,36]. This last point is illustrated in Fig. 19, which displays the convective field for $\tau = -10$, 0, and $+10$. Up to rotation rates comparable to the critical value for the
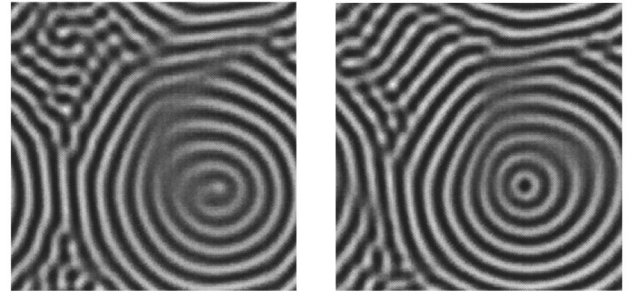

FIG. 16. Transition between a spiral and a target for $P = 2$, $\tau = 10$, $\Gamma = 16$, $\widetilde{\epsilon} = 0.1$, and free-slip boundary conditions.

onset of the Küppers-Lortz instability, we observe a progressive ''relaminarization'' of the flow, characterized by the gliding and annihilation of dislocations, and leading to a highly correlated pattern in the form of quasiparallel rolls [Fig. 18(c)]. In the presence of lateral boundaries, this phenomenon is less conspicuous due to the continuing formation and annihilation of dislocations on the sidewalls [26]. These defects were shown to be responsible for the appearance of the Küppers-Lortz instability for rotation rates below the theoretical value for its onset [7,8]. A maximum of the correlation length around τ_{KL} is nevertheless visible in experimental results for a large aspect ratio cell reported in Fig. 4 of Ref. [37], although the authors do not stress this point. We observe in Fig. 20 that the rotation rate (normalized by the critical rotation τ_{KL}) at which the relaminarization is most
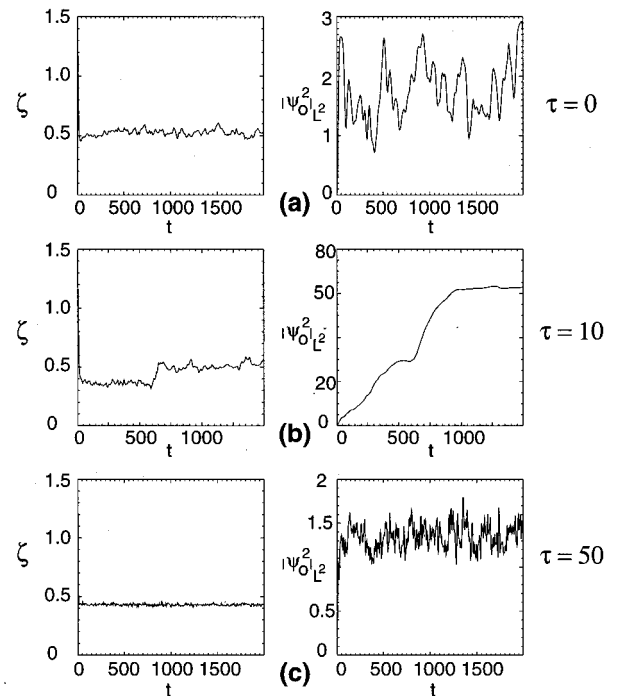

FIG. 17. Time evolution of the correlation length ζ defined by Eq. (4.2) (left) and of the L^2 norm of the mean flow stream function (right) for free-slip boundary conditions, with $P = 1.2$, $\widetilde{\epsilon} = 0.7$, and rotation rates $\tau = 0$ (a), $\tau = 10$ (b) and $\tau = 50$ (c).
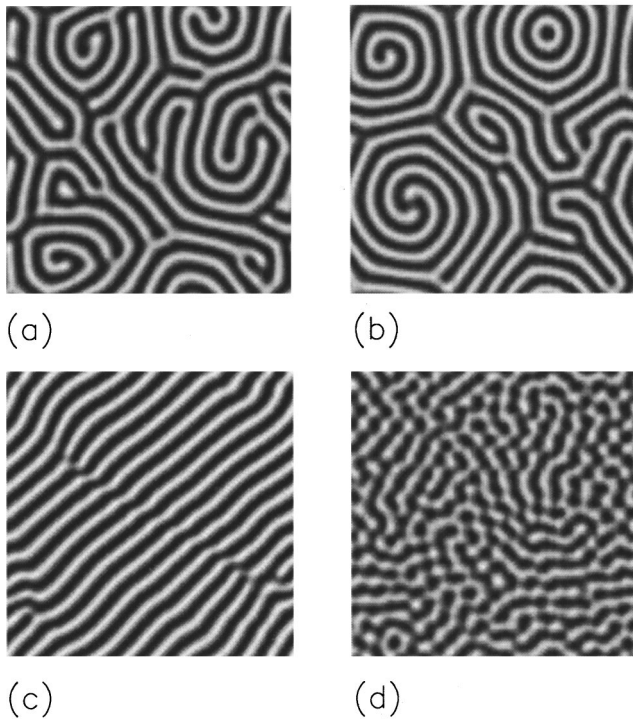
FIG. 18. Convective pattern for rigid boundary conditions, with $P=1.2$ and $\widetilde{\epsilon}=0.7$, and $\tau=0$ (a), $\tau=10$ (b), $\tau=40$ (c) and $\tau=56$ (d).

efficient, increases as the Prandtl number is reduced. Note that the quasistraight roll patterns obtained after the relaminarization process, are still subject to the KL instability, but the value of τ being close to τ_{KL}, the patches have a size comparable to that of the container. As a result, the rolls rotate globally, keeping a high degree of correlation. In Fig. 21, we display the correlation length ζ and L_2 norm of the stream function ψ_0 for $P=1.2$, $\widetilde{\epsilon}=0.7$, and various rotation rates $\tau=0$, 10, and 40. The striking features are (i) the decrease of the L^2 norm of the mean flow with time (although not monotonic) and (ii) the anticorrelation between ζ and $|\Psi_0|_{L_2}$, especially visible for $\tau=40$. The gradual decrease of $|\Psi_0|_{L_2}$ for $\tau=0$ is consistent with the formation of spirals and targets for which the mean flow is minimum. Although the system is not a gradient flow, it evolves as if it were trying to maximize the heat transport by creating structures for which the friction of the horizontal flow on the top and bottom boundaries is minimized. For nonzero rotation rates, the formation of very correlated structures (almost straight rolls) also corresponds to a minimization of the mean flow. It is noticeable that with free-slip boundaries, this tendency is exactly the opposite. In the latter case, the coherent structures formed at $\tau=10$, correspond to targets which maximize the mean flow [Fig. 17(b)]. Finally, when the Küppers-Lortz instability is efficient, a highly chaotic regime is recovered [Fig. 18(d)].

We conclude this section by mentioning that a transition between spiral chaos and a stationary pattern of straight parallel roll was recently observed in convection experiments performed in the absence of rotation in a square cell with a fluid of Prandtl number one, in a range of parameters for
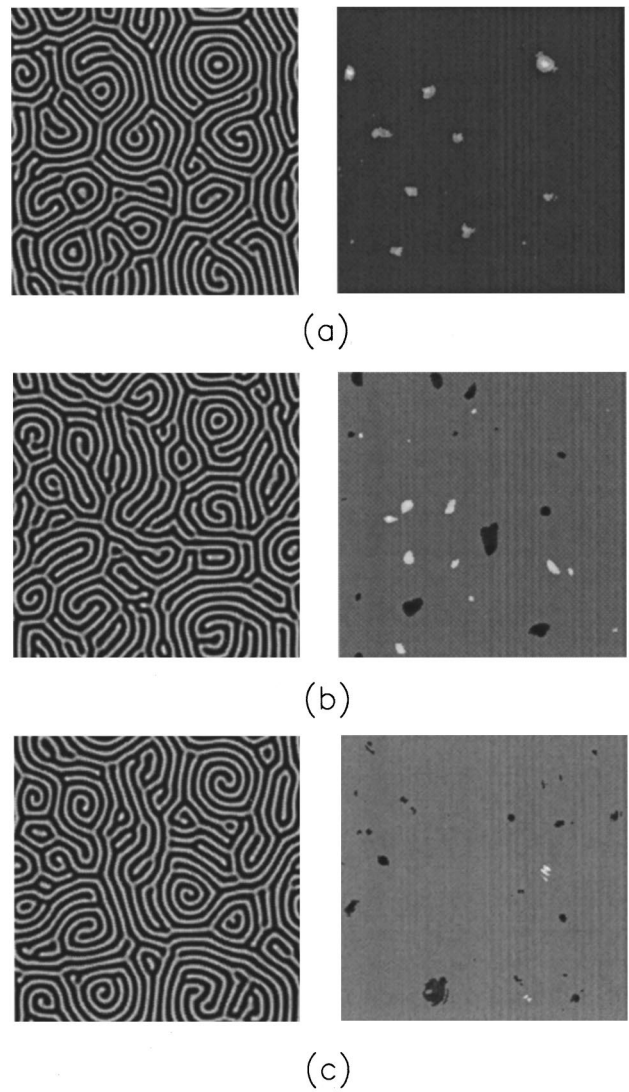

FIG. 19. Convective pattern (left) and mean flow stream function filtered by the condition $|\Psi|>\sup|\Psi|/3$ (right) for rigid boundary conditions $P=1.2$ and $\widetilde{\epsilon}=0.7$, and $\tau=10$ (a), $\tau=0$ (b) or $\tau=-10$ (c), showing positive or negative vortex cores according to the sign of τ.
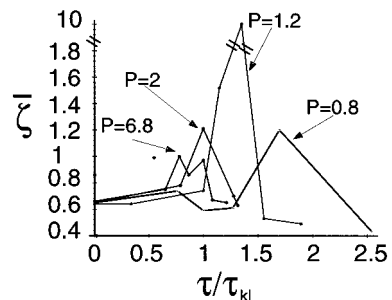

FIG. 20. Time average of the correlation length $\overline{\zeta}$ vs the rotation rate τ normalized by the critical value τ_{KL} for onset of the Küppers-Lortz instability, for different Prandtl numbers.
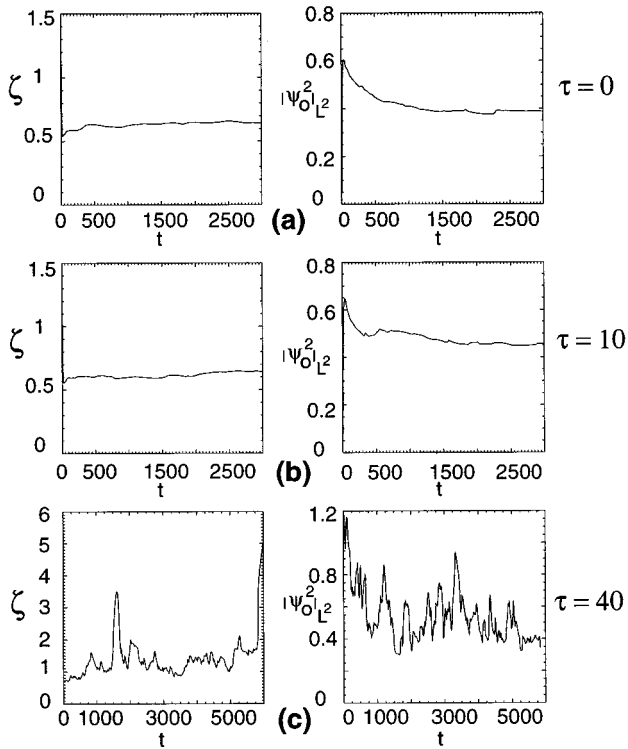
FIG. 21. Time evolution of the correlation length ζ (left) and of the squared L^2-norm of the mean flow stream function (right) for rigid boundary conditions $P=1.2$ and $\tilde{\epsilon}=0.7$, and different rotation rates $\tau=0$ (a), $\tau=10$ (b), and $\tau=40$ (c).

which straight parallel rolls are stable in an infinite medium [38]. After convection in the system has been initialized by a jump from below onset ($\epsilon<0$) to above onset ($\epsilon>0$), formation of straight parallel rolls was observed near the sidewalls, while a random pattern appears in the middle of the cell. If ϵ is not too large, a competition between patches of

spiral chaos and of straight parallel rolls develops, and, in some instances, a patch of straight parallel rolls grows and fills the entire cell. This situation contrasts with experiments in cylindrical boxes where the roll tendency to align perpendicularly with the boundaries, results in roll curvature and, under the mean flow effect, leads to a persistent spiral chaos. In this context, the question arises whether there exits a relation between the above transition and the relaminarization observed in our rotating convection model, the enhancement of the defect motions due to rotation promoting faster relaminarization.

VI. SUMMARY

A Swift-Hohenberg-type model was derived for rotating convection at a finite Prandtl number with free-slip or rigid boundary conditions. Rotation is shown to reduce the friction coefficient of the mean flow on the rigid top and bottom boundaries, and the nonlinear couplings are adjusted in such a way as to accurately reproduce both the zigzag and Küppers-Lortz instabilities. Numerical integration in the case of a periodic horizontal geometry points out the relaminarization effect of a moderate rotation which counterbalances the destabilizing influence of the mean flow. This is mostly a consequence of the enhanced gliding of the dislocations which, in periodic geometries, can totally annihilate each other. With rigid boundaries, this leads to the reformation of straight parallel rolls, while in the case of free-slip boundary conditions these structures, destabilized by the small-angle instability, evolve toward large coherent targets embedded in small-scale turbulence.

[1] M. C. Cross and P. C. Hohenberg, Science **263**, 1569 (1994).
[2] G. Küppers and D. Lortz, J. Fluid Mech. **35**, 609 (1969).
[3] R. M. Clever and F. H. Busse, J. Fluid Mech. **94**, 609 (1979).
[4] G. Küppers, Phys. Lett. **32A**, 7 (1970).
[5] T. Clune and E. Knobloch, Phys. Rev. E **47**, 2536 (1993).
[6] Y. Ponty, T. Passot, and P. L. Sulem, Phys. Fluids **9**, 67 (1997).
[7] F. Zhong, R. Ecke, and V. Steinberg, Physica D **51**, 596 (1991).
[8] J. Millán-Rodríguez and C. Pérez-García, CHAOS **4**, 369 (1994).
[9] Y. Hu, R.E. Ecke and G. Ahlers, Phys. Rev. E **55**, 6928 (1997).
[10] M. Neufeld, R. Friedrich, and H. Haken, Z. Phys. B **92**, 243 (1993).
[11] M. Fantz, R. Friedrich, M. Bestehorn, and H. Haken, Physica D **61**, 147 (1992).
[12] J. Millán Rodríguez, C. Pérez-García, M. Bestehorn, M. Fantz, and R. Friedrich, Phys. Rev. A **46**, 4729 (1992).
[13] S. Chandrasekhar, *Hydrodynamic and Hydromagnetic Stability* (Oxford University Press, London, 1961).
[14] Hao-wen Xi, J. D. Gunton, and G. A. Markish, Physica A **204**, 741 (1994).
[15] F. H. Busse and E. W. Bolton, J. Fluid Mech. **146**, 115 (1984).
[16] A. Zippelius and E. D. Siggia, Phys. Fluids **26**, 2905 (1983).
[17] P. Manneville, J. Phys. (France) **44**, 759 (1983); **44**, 903 (1983).
[18] A. J. Roberts, J. Aust. Math. Soc. B, Appl. Math. **34**, 174 (1992).
[19] H. S. Greenside and M. C. Cross, Phys. Rev. A **41**, 2492 (1985).
[20] Hao-wen Xi and J. D. Gunton, Phys. Rev. E **52**, 4963 (1995).
[21] M. C. Cross, D. Meiron, and Y. Tu, CHAOS **4**, 607 (1994).
[22] A. C. Newell, T. Passot, and M. Souli, J. Fluid Mech. **220**, 187 (1990).
[23] M. C. Cross and A. C. Newell, Physica D **10**, 299 (1984).
[24] A.C. Newell, T. Passot, N. Ercolani, and R. Indik, J. Phys. II **5**, 1863 (1995).
[25] F. H. Busse and K. E. Heikes, Science **208**, 173 (1980).
[26] Y. Ponty, T. Passot, and P. L. Sulem, Phys. Rev. Lett. **79**, 71 (1997).

[27] H. Xi, J. D. Gunton, and J. Viñals, Phys. Rev. Lett. **71**, 2030 (1993).

[28] S. W. Morris, E. Bodenschatz, D. S. Cannell, and G. Ahlers, Phys. Rev. Lett. **71**, 2026 (1993).

[29] W. Decker, W. Pesch, and A. Weber:, Phys. Rev. Lett. **73**, 648 (1994).

[30] Y. Hu, R. Ecke, and G. Ahlers, Phys. Rev. Lett. **74**, 391 (1995).

[31] Y. Hu, R. Ecke, and G. Ahlers, Phys. Rev. E **51**, 3263 (1995).

[32] M. Assenheimer and V. Steinberg, Nature (London) **367**, 345 (1994).

[33] S. W. Morris, E. Bodenschatz, D. S. Cannell, and G. Ahlers, Physica D **97**, 164 (1996).

[34] M. Cross, Physica D **97**, 65 (1996).

[35] R. E. Ecke, Y. Hu, R. Mainieri, and G. Ahlers, Science **269**, 1704 (1995).

[36] W. Pesch, CHAOS **6**, 348 (1996).

[37] Y. Hu, R. Ecke, and G. Ahlers, Phys. Rev. Lett. **74**, 5040 (1995).

[38] R. V. Cakmur, D. A. Egolf, B. P. Plapp, and E. Brodenschatz (unpublished).